Hindawi
Advances in Civil Engineering
Volume 2024, Article ID 5119809, 15 pages
https://doi.org/10.1155/2024/5119809

Research Article

Research on 3D Measurement and Rapid Location Technique for Assembling the Special-Shaped Structural Segments

Shilei Wang[1], **Zhangming Wang**[2] **and Qiankuan Feng**[1]

[1]*Infrastructure Inspection Research Institute, China Academy of Railway Sciences Group Co. Ltd., Beijing 100081, China*
[2]*CCCC Highway Bridges National Engineering Research Centre Ltd., Beijing 100088, China*

Correspondence should be addressed to Qiankuan Feng; fqk@rails.cn

Received 5 July 2022; Revised 3 February 2024; Accepted 5 February 2024; Published 26 February 2024

Academic Editor: Angelo Aloisio

The pylon of the Xinshougang Bridge, a welded steel box arch with a variable cross-section, exhibits asymmetrical design and unevenly inclined limb ends. The segmented assembly of this uniquely shaped steel pylon necessitates precise splicing. In this paper, a novel three-point method for segment attitude positioning is proposed based on the local coordinate system. This method facilitates accurate coordinate translation and attitude alignment between the section preparation facility and the construction site. Furthermore, a predictive methodology for segment posture during erection is introduced, aiming to minimize misalignments at the connection interfaces. This approach accounts for potential deviations arising in manufacturing and erection phases. The synergistic application of these methods effectively ensures the precise geometric shape of the bending and twisting steel tower throughout its phased construction.

1. Introduction

With the advent of rapid urbanization in the 21st century, the expansion of bridges in urban areas has accelerated [1–3]. These structures have evolved beyond their fundamental role in transportation, acquiring additional symbolic significance and cultural meaning. Consequently, there has been a growing demand for esthetic enhancement of bridges. This trend has particularly highlighted the importance of special-shaped steel pylon cable-stayed bridges, renowned for their intricate designs and visual appeal, which have garnered significant interest in the field of urban architecture [4, 5].

For the accuracy and esthetic integrity of bridge structures, stringent construction precision is mandatory in the construction of complex-shaped steel pylons. The erection or assembly of large scale, uniquely shaped structures typically involves segmental processes. However, this approach presents significant challenges in engineering surveying, notably in the precise positioning and error adjustment of segments [6, 7].

During the installation and positioning of these special-shaped segments, it is crucial to ensure the axial deviation of the segment within permissible limits [8, 9]. The axis, serving as a virtual control target, cannot be measured directly. Instead, it requires a transformation and representation based on the coordinate errors of multiple feature points on the segment's surface [10]. The complexity is heightened in long-span bridges, often featuring pylons exceeding 100 m in height, complicating the measurement tasks.

In practice, the 3D scanning technology that allows the direct acquisition of coordinates of feature points on the surface, often struggles to meet the stringent precision requirements [11, 12]. For vertical and regular-shaped structures, technologies like total stations and GPS are employed to acquire the coordinate data of surface feature points [13–15]. This method necessitates placing targets at each feature point, and setting a conversion relationship between the target measurement center and the segment's surface feature points. The spatial position of each special-shaped structure segment relative to the measurement coordinate system changes constantly,

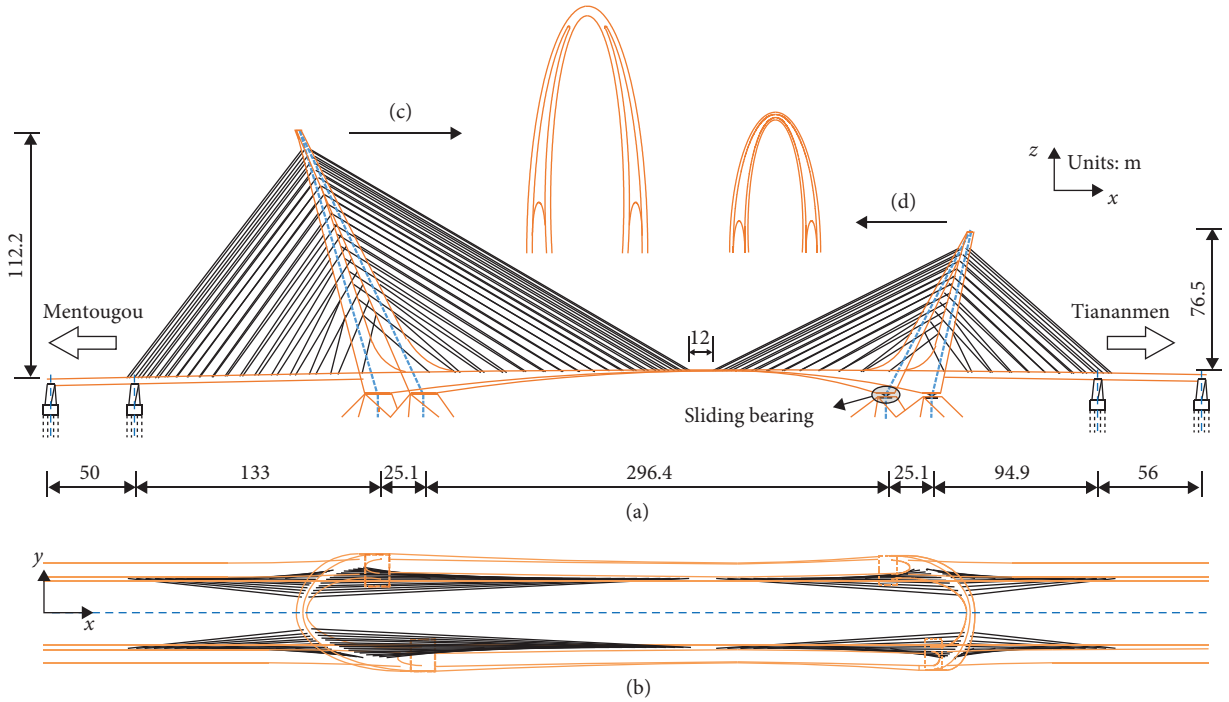

Figure 1: Sketch of the Xinshougang Bridge [25]: (a) main view; (b) top view; (c) side view of the high pylon; and (d) side view of the low pylon.

which poses a challenge in establishing a consistent measurement coordinate conversion relationship [16–18].

To address these challenges, various methods have been developed. Specifically, a tool for measuring the coordinates of feature points on the surface was developed, aiding in the erection of the inclined steel pylon of Nanjing Yangtze River Bridge [19]. Moreover, a method leveraging analytical and rotation matrix approaches for positioning feature point coordinates was formulated for the erection of bending–torsion components in the National Stadium (colloquially known as the Bird's Nest) [20]. Additionally, a method for measurement and positioning of virtual tetrahedron vertex was proposed for facilitating the erection of multi-member tubular weld joints in Zhejiang Art Museum [21].

In the assembly of vertical pylon segments, a weighted evaluation is typically employed to estimate the deviation of the upper port axis. According to the installation positions of the instrument, this process can be categorized into two methods: internal control method and external control method. The internal control method involves setting up the measuring instrument directly on the current segment, with the points to be measured situated within a measurement control network of the same set of control points. This method, characterized by shorter distances between the measuring instrument and the measured points, ensures high-measurement accuracy. However, it necessitates arranging measuring stations on the segment and faces challenges in implementation, especially when the upper port is inclined or in high, wind-prone environments. The external control method, in contrast, entails positioning the instrument on a ground control point and placing targets on the segment's upper port points to be measured. This method may require altering the measuring station in response to on-site structural panels or other construction factors, aiming to complete the coordinate collection of all feature points. It is, however, less accurate than the internal control method [22].

Taking the Xinshougang Bridge as the engineering background [23–25], this paper proposes a novel method for transferring the coordinates of multiple feature points by three observation points from prefabrication plant to erection site. This technique aims to control the erection precision of arch-shaped, variable-section bending–torsion steel pylon by segment. Furthermore, the paper proposes a predictive approach for determining the posture of segments to be erected, designed to minimize planar misalignment at connection interfaces. This approach holistically accounts for deviations encountered during both fabrication and erection phases. It serves as a guidance tool for segment fabrication, erection, and adjustment processes, proving effective in controlling the erection precision of bending–torsion steel pylons by segment. In light of this, the successful deployment of the two methods in the Xinshougang Bridge has played a pivotal role in geometry control of the bending and twisting steel pylon, showing their effectiveness and utility in the real-world scenarios.

2. Engineering Background

2.1. Bridge Characteristics. The Xinshougang Bridge, situated west of Chang'an Street in Beijing and spanning the Yongding River. This bridge features a five-span, high-low dual-pylon, cable-stayed rigid-frame continuous beam composite system, constructed with Q420e steel. It spans a total length of 639 m, with a main span of 280 m, as illustrated in Figure 1.

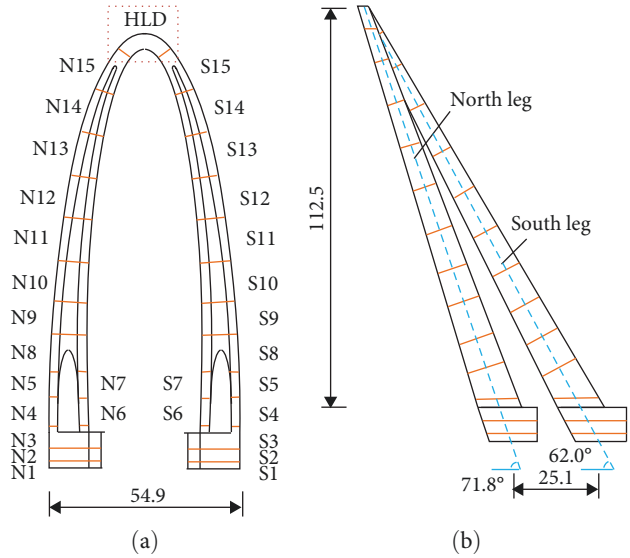

Figure 2: Different views of high pylon. (a) Transverse direction of bridge. (b) Longitudinal direction of bridge.

It stands as the world's tallest steel arch pylon cable-stayed bridge. Its pylons, characterized by a sloping arch design, align at a skew angle of 57.40° relative to the river's centerline, diverging from the bridge's centerline. This unique design, adapting to the river's flow direction, results in pylons with nonuniform inclinations, creating a visually impactful "stepping" effect and a spatially distorted appearance. The bridge's esthetic and innovative design earned it the prestigious Eugene C. Figg Jr. Medal at the 2020 International Bridge Conference (IBC), celebrating its beauty, revolutionary approach, and the iconic status it provides to the community it serves.

2.2. Steel Pylon Features. The bridge's steel pylon is a sophisticated architectural feat, being an all-welded steel box arch with variable cross-segments. It exhibits nonuniform tilting of limbs and asymmetric torsion in space. The taller pylon stands at a height of 123.780 m and weighs approximately 9,850 t. The inclination angles of the pylon legs differ, with the north leg at 71.8° and the south leg at 62.0°. Spanning a distance of 25.100 m along the bridge, the pylon's north and south limbs are segmented into 15 sections each, totaling 31 segments, including the closure segments, as illustrated in Figure 2. All segments are welded in the factory and assembled at the bridge sites. The steel pylon is erected based on the bracket-assisted installation method [16].

The control standard of steel pylon design axis deviation is $H/4{,}000$, where H denotes the height of the pylon. The allowable deviation at the top of the pylon is about 31 mm, and the allowable deviation of elevation is $\pm 2n$ within 20 mm, where n denotes the segment number. The single-limb steel pylon of the background bridge, when projected along the bridge direction, displays a linearly inclined profile with a variable cross-section. In contrast, the projection across the bridge manifests as an elliptical profile, also with a variable cross-section. The axis of each segment forms a composite spatial curve, integrating oblique straight lines along the bridge with elliptical curves across it. The interface surface of each segment aligns perpendicularly to the tangent of this spatially curved axis. Consequently, the lower interface of each segment presents as a spatially inclined plane within the geodetic coordinate system.

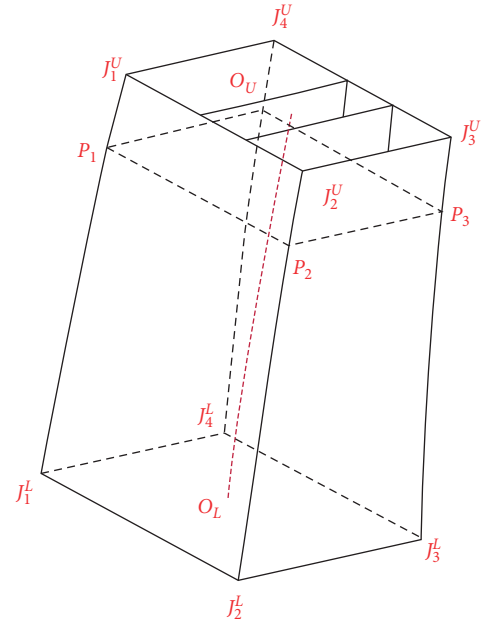

Figure 3: Layout of geometry control feature points.

3. Segment Positioning

3.1. Geometric Feature Point Layout. The layout of geometric control points for the single segment is shown in Figure 3. The selection of geometric morphological feature points should reflect the three-dimensional characteristics of the pylon segment. Based on these feature points, the manufacturing and

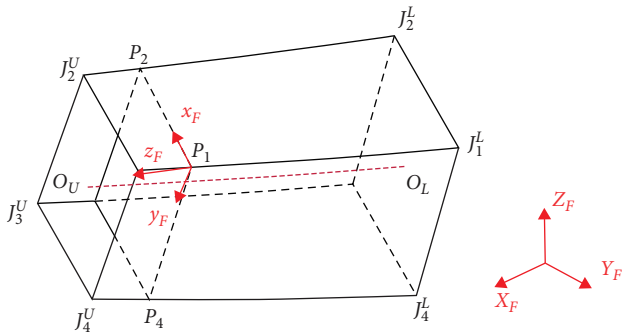

FIGURE 4: Layout of coordinated systems.

processing status of both the upper and lower interfaces of the segment can be evaluated. In addition, the deviation of the axis is a key comprehensive index for assessing the erection accuracy in manufacturing, so geometric control points should encompass the pivot points of the segment's upper and lower interfaces.

There are 13 control points of the single segment geometry. J_i^U represents the upper interface control points of the segment, while J_i^L denotes the lower interface control points. These control points are strategically positioned at the intersections of the segment's outer wall panels, where coordinates are readily obtainable. O^U and O^L are the pivot points for the upper and lower interfaces of the segment, respectively, and located in the virtual space.

P_i is a relatively flexible measuring point, typically set near the outer intersection of the first transverse partition of the upper interface and the four-sided wall panel. This placement is due to the consideration of the rigidity, which ensures the relative stability of each P_i. The distance between these measuring points and the upper interfaces usually ranges from 0.5 to 1.5 m, and the deformation of the upper interface relative to the diaphragm is negligible.

3.2. Three-Point Method. The factory coordinate system designated as $(OXYZ)_F$ is constructed, based on three measuring points P_1–P_3 situated near the upper interface of the segments. All the feature points on the segment can be encapsulated into $(OXYZ)_F$ constructed by these three points. The local coordinate system, labeled as $(oxyz)_F$, is anchored at point P_1. Its x-axis oriented from point P_1 toward point P_2. The z-axis is perpendicular to the plane formed by the trio of measuring points P_1–P_3, ensuring a multidimensional perspective. Furthermore, the y-axis is determined by the right-hand rule. The layout of the segment coordinate system is illustrated in Figure 4.

The calculation method for converting the factory coordinate system $(OXYZ)_F$ to the local coordinate system $(oxyz)_F$ is shown in Equation (1):

$$(x, y, z)_F^T = R_F((X, Y, Z)_F^T + T_F), \tag{1}$$

where R_F and T_F represent the rotation matrix and translation vector, which can be derived from Equation (2):

$$R_F = \begin{bmatrix} u_{xi}^{(F)} & u_{xj}^{(F)} & u_{xk}^{(F)} \\ u_{yi}^{(F)} & u_{yj}^{(F)} & u_{yk}^{(F)} \\ u_{zi}^{(F)} & u_{zj}^{(F)} & u_{zk}^{(F)} \end{bmatrix}, T_F = [-X_{P1F}, -Y_{P1F}, -Z_{P1F}]^T, \tag{2}$$

where $\{X_{P1F}, Y_{P1F}, Z_{P1F}\}$ represent the coordinates of the origin P_1 in $(OXYZ)_F$, $\{u_x^{(F)}, u_y^{(F)}, u_z^{(F)}\}$ represents the local coordinate vector of the x-axis, y-axis, and z-axis of $(oxyz)_F$ in $(OXYZ)_F$. The calculation method is shown in Equation (3).

$$u_x^{(F)} = \frac{\overrightarrow{P_1P_2}}{\left|\overrightarrow{P_1P_2}\right|}, u_z^{(F)} = \frac{\overrightarrow{P_1P_2} \times \overrightarrow{P_1P_3}}{\left|\overrightarrow{P_1P_2} \times \overrightarrow{P_1P_3}\right|}, u_y^{(F)} = u_x^{(F)} \times u_z^{(F)}, \tag{3}$$

where $\overrightarrow{P_1P_2}$ and $\overrightarrow{P_1P_3}$ are calculated in the $(OXYZ)_F$ coordinate system.

In the erection phase of the segments, the same principles for coordinate conversion are applicable. The geometric coordinate system is designated as $(OXYZ)_G$, and a similar geometric local coordinate system, termed $(oxyz)_G$, is established. It is important to note that local structural deformations may cause minor position shifts among points near the upper interface; however, these deviations are typically negligible. Consequently, for any point of the interface, $(x, y, z)_F = (x, y, z)_G$. Furthermore, the relationship for transferring coordinates of any point between the two systems, $(OXYZ)_F$ and $(OXYZ)_G$, is quantified and presented in Equation (4). This relationship facilitates accurate and consistent coordinate translation between the two systems, ensuring precise alignment and positioning of the segments throughout the construction process.

$$(X, Y, Z)_G^T = R_G^{-1}(x, y, z)_G^T - T_G = R_G^{-1}(x, y, z)_F^T - T_G. \tag{4}$$

Figure 5(a) describes the relationship of the coordinate system during the erection. When the relationship between the upper interface feature points and three measuring points P_1–P_3 is established in the factory, the P_1–P_3 points and the upper interface pivot points can be further established based on spatial attitude estimation relation.

During on-site erection, it suffices to collect the coordinates of points P_1–P_3 to ascertain the axis coordinates of the upper interface within the geometric coordinate system. By comparing these coordinates with the target coordinates, the positioning status of the upper interface's pivot point can be determined, thus providing essential data for assessing or adjusting the segment's posture.

In fact, the reasonable arrangement of measuring points can accomplish the simultaneous collection of coordinates for three points P_1–P_3 from a single station. This approach effectively circumvents the need to change stations while collecting all feature points of the upper interface, thereby enhancing the efficiency of measurement and control. Figure 5(b) exhibits

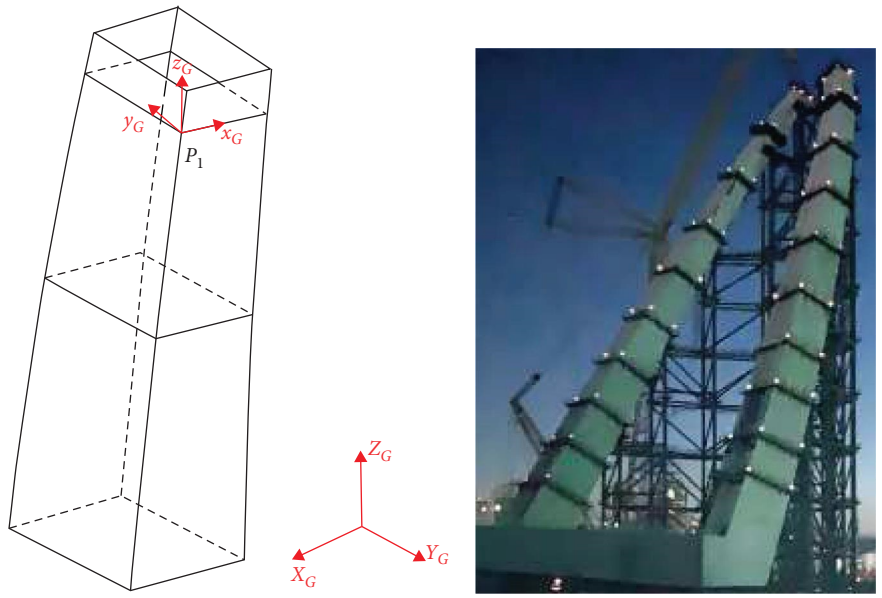

(a) (b)

FIGURE 5: Points layout during the erection. (a) Relationship of the coordinate system. (b) Point positions in the actual structure.

the layout of on-site measurement points for the steel pylon of the bridge. These points are instrumental not only in the posture positioning of the segments but also serve as interfaces for observing segment deformation. This comprehensive measurement strategy is crucial for ensuring the precision and stability of the structure during construction.

3.3. Error Analysis. The calculation method for the conversion of coordinates between the factory coordinate system $(OXYZ)_F$ and the geodetic coordinate system $(OXYZ)_G$ can be obtained by substituting Equation (1) into (4). The coordinate $(X, Y, Z)_G$ based on the three-point positioning method can be calculated in Equation (5):

$$(X, Y, Z)_G^T = R_G^{-1} R_F ((X, Y, Z)_F^T + T_F) - T_G. \tag{5}$$

Due to the proximity of factory measurements, environmental factors and distortions within the reference network are minimized, resulting in a high level of measurement precision. It can be considered that the transformation error from the factory coordinate system $(OXYZ)_F$ to the local coordinate system $(oxyz)_F$ is negligible. Furthermore, it can be assumed that $(oxyz)_F$ and $(oxyz)_G$ are the same coordinate system, while the factory coordinate system $(OXYZ)_F$ is the measured error free state. Following this assumption, the deviation of a point's coordinates on the upper interface can be accurately assessed using the coordinates of points P_1–P_3 in the geodetic coordinate system, as following:

$$\begin{aligned}(\Delta X, \Delta Y, \Delta Z)^T &= (X, Y, Z)_G^T - (X, Y, Z)_F^T \\ &= R_G^{-1}(x, y, z)_F^T - T_G - (X, Y, Z)_F^T.\end{aligned} \tag{6}$$

The measurement points P_1–P_3 are determined using total station measurements, stationed at the observation posts within the control network. The precision of single-point coordinates is subject to various factors, including atmospheric refraction and the accuracy of the instrumentation.

The error distribution can be visualized as a path traced by polar coordinates, with an undefined point O serving as the pole, ψ representing the polar angle, and σ_ψ denoting the radial distance, as depicted in Figure 6(a). An ellipse, which closely approximates the shape of the error curve, is typically employed as a substitute. Given the random distribution characteristics of measurement errors, it is assumed that the measurement points P_1–P_3 are scattered randomly across the error ellipse, as illustrated in Figure 6(b). This probabilistic approach to error distribution allows for a more pragmatic and manageable analysis of measurement inaccuracies.

Based on the defined error ellipse, the maximum error for a particular point, such as the interface pivot point O_U, calculated by these three points, can be pinpointed. This calculated error can be evaluated for the applicability of calculating the O_U point based on P_1–P_3. The mathematical calculation model for finding the maximum error of the point O_U under a feature measuring point layout scheme can be required in Equation (7):

$$\begin{aligned}&\max f(\cdots, P_{ixe}, P_{iye}, P_{ize}, \cdots) = (\Delta X, \Delta Y, \Delta Z)^T \\ &= \left| R_G^{-1}(x, y, z)_F^T - T_G - (X, Y, Z)_F^T \right|,\end{aligned} \tag{7}$$

where P_{ixe}, P_{iye}, and P_{ize} represent the coordinate P_i situated on the ellipse error trajectory. These coordinates must comply with the specific constraints imposed by the elliptical shape on a plane, and their elevation must fall within the error margin designated for P_i. The constraint condition that the objective function must fulfill is detailed in Equation (8):

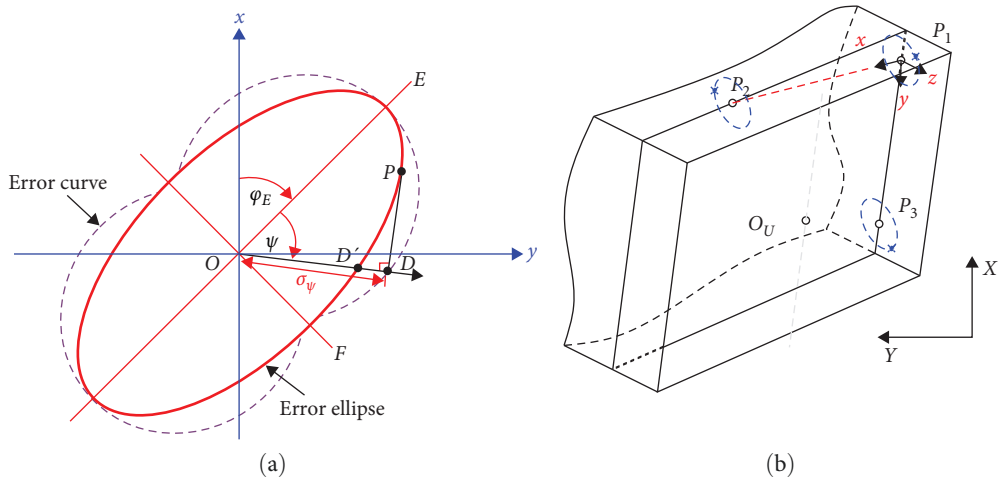

Figure 6: Error ellipse and error distribution. (a) Single point error ellipse. (b) Multipoint error distribution.

Table 1: Survey and adjustment results of GTN15.

Point name	Coordinate after adjustment (m)			Geodetic error component (mm)			Error ellipse parameter		
	N	E	H	N	E	H	E (mm)	F (mm)	φ_E (degree)
D2	704.033	362.833	83.289	0.0	0.0	0.0	0.0	0.0	0.0
A2	544.083	234.071	83.706	0.0	0.0	0.0	0.0	0.0	0.0
B1	363.842	460.113	81.018	0.0	0.0	0.0	0.0	0.0	0.0
GTN15-P_1	484.987	197.463	205.782	1.7	1.9	2.4	2.0	1.6	147.4
GTN15-P_3	481.403	198.800	203.355	1.7	2.0	2.4	2.1	1.6	147.5
GTN15-P_2	485.402	194.224	205.304	1.7	2.0	2.4	2.1	1.6	147.5

$$s.t.\begin{cases} (x_i - P_{ix})^2 + (y_i - P_{iy})^2 - \dfrac{c^2\sin(2\theta)(x_i - P_{ix})(y_i - P_{iy})}{a^2 - c^2\cos^2\theta} = \dfrac{a^2b^2}{a^2 - c^2\cos^2\theta}, \\ -\Delta Z \le z_i \le \Delta Z \end{cases} \tag{8}$$

Repeating algorithm for calculating errors with P_1–P_3. By altering the configuration of points P_1–P_3, one can analyze the error variation patterns of the pivot point O_U and the sensitivity of the corresponding parameters. This analysis is instrumental in guiding the determination of the optimal error for O_U points and in optimizing the arrangement of P_1–P_3 points [26–28].

3.4. Layout Optimization. To analyze the error of the north pylon's 15th section's upper interface axis coordinate (GTN15), a total station was established at station D2, with back sight points A2 and B1. The maximum observation distance is about 302 m. The coordinates are measured by Leica TS60, and the adjustment of the measurement results is completed by the Leica multireturn data analysis system, as shown in Table 1. The control network shape and error ellipse distribution are shown in Figure 7(a), and the actual layout of points U_0 and P_1–P_3 on the upper interface is shown in Figure 7(b). The maximum distance between the three points is only 6.38 m, the maximum long semi-axis is 2.1 mm, and the maximum short semi-axis is 1.6 mm. The angle between the long axis of the error ellipse and the geodetic coordinate system is $\varphi_E = 147.5°$.

Based on the above-mentioned measured error ellipse parameters, this section studies the estimated maximum deviation of U_0 and its influencing factors under different P_1–P_3 layout schemes, so as to control the maximum deviation of U_0 by optimizing the layout of P_1–P_3.

It is essential to ensure that the layout of P_1–P_3 allows for measurement completion from a single test station; switching stations would lead to significant inconvenience and uncertainty in measurement errors. Based on this principle, different potentially feasible arrangements of P_1–P_3 are shown in Figure 8.

Points P_1–P_3 are positioned on the outer edge of the junction between the diaphragm and the surrounding wall panels. Taking visibility into account, the travel routes of P_1–P_3 points between J_1–J_4 corner points are set, and a total of three types of work are investigated. The main points of each working condition are as follows:

In Case 1, point P_1 is located at J_4; P_1 and P_3 maintain an equal distance from J_4 until P_3 reaches J_1. The angle between P_1–P_3 is kept constant.

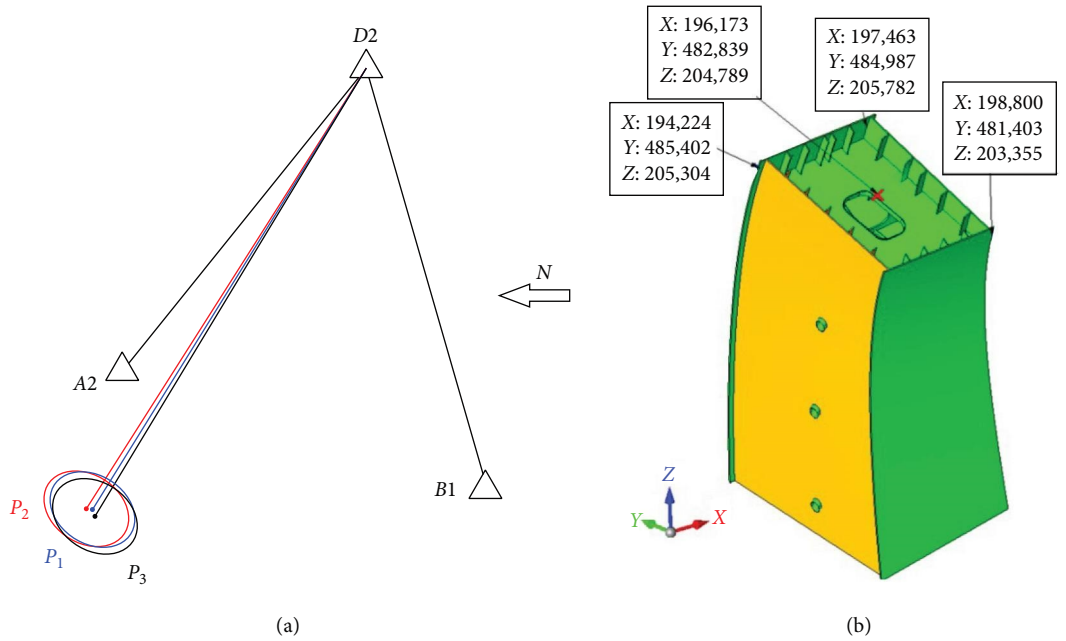

Figure 7: Configuration of survey control network and adjustment results. (a) Control network shape and survey adjustment. (b) GTN15 upper interface form.

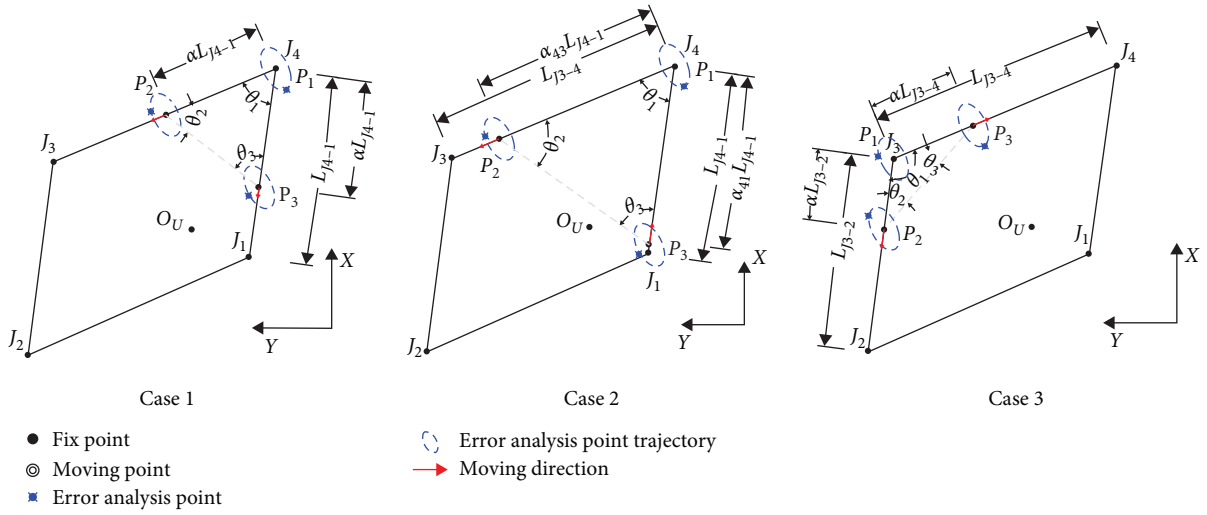

Figure 8: Different arrangements of P_1–P_3.

In Case 2, point P_1 is located at J_4; P_3 travels from J_1 to J_4; point P_2 travels to J_3, and the area of the triangle formed by points P_1–P_3 is unchanged.

In Case 3, point P_1 is located at J_3; points P_1 and P_3 travel from J_3 to J_2, J_4 along the same distance scaling factor α. At $\alpha = 1$, the area of the triangle formed by P_1–P_3 is maximized.

The calculation results of Case 1–Case 3 are shown in Tables 2 and 3. S_k denotes the area of the triangle created by P_1–P_3 at the current step. Max/Min (θ) is the maximum and minimum angle ratio of the current triangular configuration. Max (S_k)/S_k is the ratio of the maximum configuration area to the current configuration area of all steps. $\delta = \Delta U/\Delta P$ the ratio of the maximum coordinate deviation estimated in the current step to the maximum point deviation ΔP of the three points P_1–P_3, among them, $\Delta P = \sqrt{\Delta^2 N + \Delta^2 E + \Delta^2 H} = 3.53$ mm.

Case 1 describes the change rule of the error ratio δ with the area ratio when the configuration angle ratio remains unchanged, and Case 2 describes the change rule of the error ratio δ with the angle ratio when the configuration area remains unchanged. As is shown in Figure 9, in the near-optimal state, the error ratio δ is basically linearly related to the intersection angle ratio or area ratio. In the range of the angle ratio or area ratio between 1.0 and 4.0, the ratio is more sensitive than the angle ratio, and the optimal error ratio

Table 2: Results of Case 1 and Case 3.

Scaling factor	S_k (10^6 mm^2)		ΔU (mm)		Max/Min (θ)		Max (S_k)/S_k		$\delta = \Delta U/\Delta P$	
α	Case 1	Case 3	Case 1	Case 3	Case 1	Case 3	Case 1	Case 3	Case 1	Case 3
0.01	0.00	0.00	798.4	688.4	1.40	3.5	10,183.0	9,890.4	226.2	195.0
0.02	0.00	0.00	399.7	345.7	1.39	3.5	2,496.7	2,492.7	113.2	97.9
0.04	0.01	0.01	171.2	173.0	1.41	3.5	630.2	622.8	48.5	49.0
0.06	0.02	0.03	113.1	114.6	1.41	3.5	278.3	276.8	32.0	32.5
0.08	0.03	0.04	99.8	85.5	1.41	3.5	156.5	156.3	28.3	24.2
0.10	0.05	0.07	67.0	67.8	1.42	3.5	99.9	99.9	19.0	19.2
0.15	0.10	0.15	52.1	44.3	1.41	3.5	44.5	44.4	14.8	12.5
0.20	0.18	0.27	38.5	32.6	1.41	3.5	25.0	25.0	10.9	9.2
0.25	0.28	0.43	25.4	25.5	1.41	3.5	16.0	16.0	7.2	7.2
0.30	0.40	0.61	20.8	20.8	1.41	3.5	11.1	11.1	5.9	5.9
0.35	0.55	0.83	17.6	17.4	1.41	3.5	8.2	8.2	5.0	4.9
0.40	0.72	1.09	15.1	14.9	1.41	3.5	6.2	6.2	4.3	4.2
0.45	0.91	1.38	13.2	13.0	1.41	3.5	4.9	4.9	3.7	3.7
0.50	1.12	1.70	11.7	11.4	1.41	3.5	4.0	4.0	3.3	3.2
0.60	1.61	2.45	11.4	9.1	1.41	3.5	2.8	2.8	3.2	2.6
0.70	2.19	3.33	9.6	7.5	1.41	3.5	2.0	2.0	2.7	2.1
0.80	2.86	4.35	8.3	5.9	1.41	3.5	1.6	1.6	2.4	1.7
0.90	3.63	5.50	7.3	5.6	1.41	3.5	1.2	1.2	2.1	1.6
1.00	4.48	6.79	6.5	5.3	1.41	3.5	1.0	1.0	1.9	1.5

Table 3: Results of Case 2.

α_{43}	α_{41}	S_k (10^6 mm^2)	ΔU (mm)	Max/Min (θ)	Max (S_k)/S_k	$\delta = \Delta U/\Delta P$
0.61	0.80	4.48	7.9	1.5	1.4	2.2
0.73	0.68	4.48	8.5	2.0	1.4	2.4
0.81	0.61	4.48	9.3	2.5	1.4	2.6
0.87	0.57	4.48	9.9	3.0	1.4	2.8
0.92	0.54	4.48	10.5	3.5	1.4	3.0
0.97	0.51	4.48	10.9	4.0	1.4	3.1
1.01	0.49	4.48	11.6	4.5	1.4	3.3

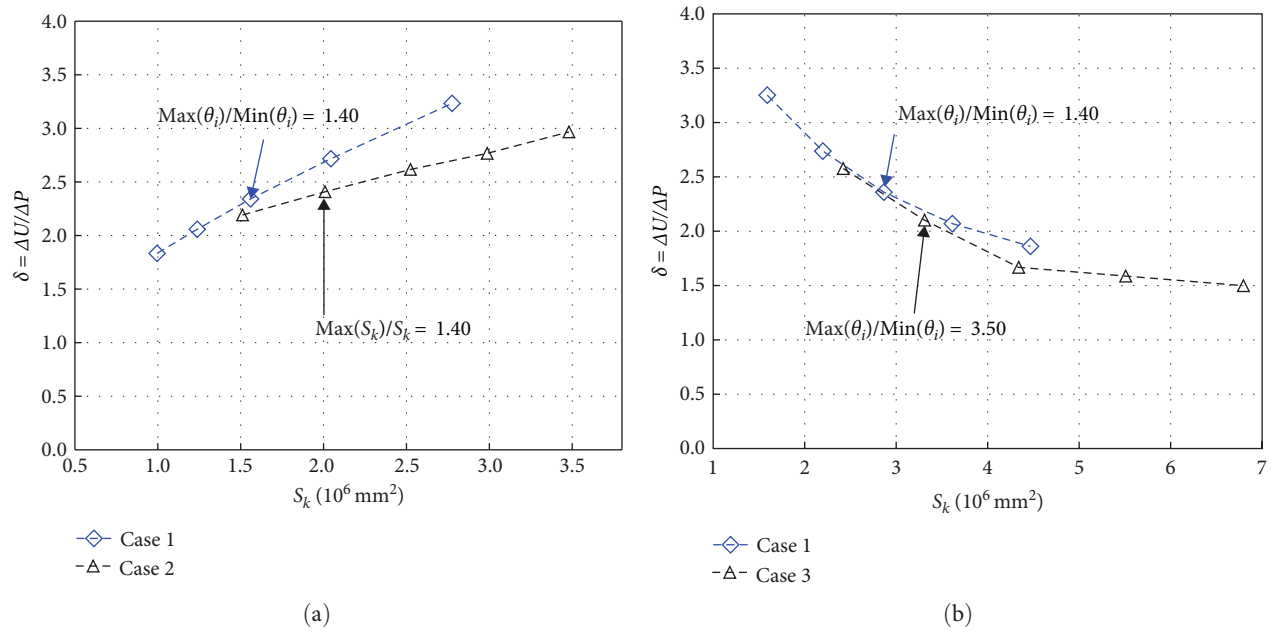

Figure 9: Relationship of error ratio δ with different factors. (a) Relationship under near-optimal state. (b) Relationship with area.

$\delta = 1.85$. If the value of calculated coordinate error ratio δ needs to be further reduced, a configuration with a larger area needs to be found in an interval with a certain intersection angle ratio. It can also be found that the error ratio δ varies nonlinearly with area.

Integrating the calculation data and the assessment of factors influencing the error ratio δ reveals that to minimize the positioning error using the three-point method for a uniquely shaped pylon, it is optimal to maximize the P_1–P_3 configuration area while ensuring the angles between these points remain uniform. This strategy enables the determination of the most suitable layout for points P_1–P_3 on the background bridge GTN15. Corresponding to the condition of $\alpha = 1.0$ in Case 3 working condition, the error ratio $\delta = 1.50$ at this time, the absolute value of point deviation ΔU is 5.3 mm. This deviation falls within the acceptable limits for the high-altitude positioning accuracy required for the steel pylon. Figure 5(b) within this document accurately represents the measuring point layout that is informed by these research findings, offering a practical application for enhancing the precision of construction methodologies.

4. Optimal Interface Misalignment

A single segment of the steel pylon is composed of surrounding wallboards, diaphragm plates, and other units fixed on the support frame. Due to the impact from welding deformation and processing deviation, segment fabrication is always subject to deviations. There is no exception to the erected segments due to impacts from welding deformation, temperature change, etc. To achieve the precise segment erection, it is vital to analyze the errors in fabrication and erection, as well as the impact on site erection. Based on the principle of minimizing the planar misalignment between connection interfaces of the target bridge, a method for predicting the posture of a segment to be erected was proposed, which comprehensively takes into account the deviations in fabrication and erection. It is used to guide the segment fabrication, erection and adjustment, and effective to control the geometry of the bending–torsion steel pylon in the segment-based erection process.

Suppose the segment to be erected and the previously erected segment are numbered by i, and $i-1$, respectively. The two segments are matched and connected through the interfaces. The misalignment between wallboards is a main index used to measure the interface matching situation. Excessive misalignment will weaken the effective stress area of weld joint, and undermine the structural stress safety. Predicting the posture of the i^{th} segment with fabrication errors under the condition that there is any deviation in erection of the $i-1^{\text{th}}$ segment, aims to find the minimal misalignment between connection interfaces. In this case, the posture predicted will be the optimal posture that is feasible on site. The amount of misalignment between wallboards can be represented by the distance between the corresponding feature points of upper and lower segments at the projection plane. In Figure 10, the blue skeleton indicates the i^{th} segment to be erected, the brown skeleton represents

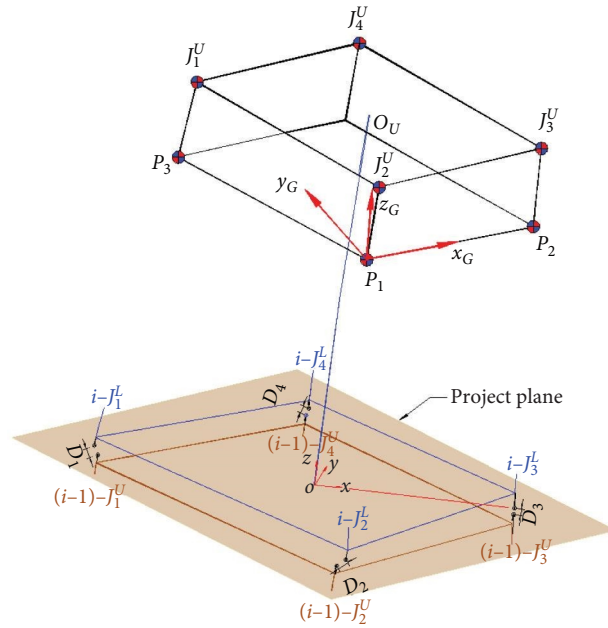

Figure 10: Sketch of align deviation.

the $i-1^{\text{th}}$ segment previously erected, and the brown plane is the upper interface plane of the $i-1^{\text{th}}$ segment. After the coordinate data of feature points of each segment are obtained by measuring the P_1–P_3 coordinates, connection interface feature points of the $i-1^{\text{th}}$ and i^{th} segments will be projected onto the interface plane, to calculate the deviation D_i of angular point misalignment between upper and lower segments. The objective function is constructed according to Equation (9).

$$\min f(\Delta X, \Delta Y, \omega_Z) = \sum\left(\left(X_{p,i-1} - X_{p,i}\right)^2 + \left(Y_{p,i-1} - Y_{p,i}\right)^2\right)^{1/2}. \tag{9}$$

In Equation (9), $\Delta X/\Delta Y$ is a translation parameter in the local coordinate system to be solved, and ω_Z is a rotation parameter in the local coordinate system to be solved. The mathematical model is designed to iteratively solve the unconstrained nonlinear single-objective function through the BFGS quasi–Newtonian variable-scale method. After the optimization parameters are obtained, it is necessary to evaluate the axial center state of the upper interface of the i^{th} segment, analyze whether the error is within the allowable range, and then invert the optimized local coordinates to geodetic coordinates. The specific inversion method is shown in Equation (9).

$$P^{(1)} = R_1^{-1}\left(R_c\left(R_1\left(P^{(0)} + T_1\right)\right) + T_c\right) - T_1, \tag{10}$$

where $P^{(0)}$represents the coordinate of the feature point of the i^{th} segment with the optimal erection posture in the geodetic coordinate system, $P^{(1)}$ indicates the coordinate of the feature point of the i^{th} segment in the geodetic coordinate

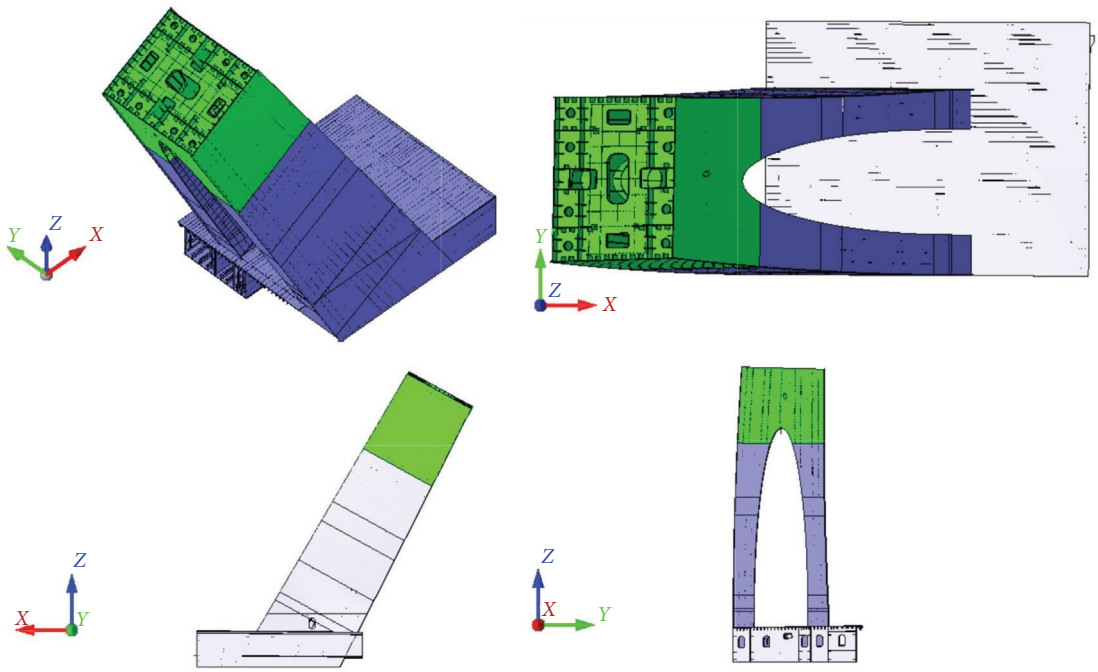

Figure 11: Different views of GTS3–8 segments.

system after the optimization in interface misalignment, R_l refers to the rotation matrix obtained after conversion from the geodetic coordinate system to the local coordinate system, and T_l denotes the translation vector obtained after conversion from the geodetic coordinate system to the local coordinate system. R_l and T_l can be calculated according to Equation (4). R_c is the rotation matrix with the optimal amount of misalignment in the local coordinate system, which can be solved according to Equation (9). T_c indicates the translation vector with the optimal amount of misalignment in the local coordinate system, which can be solved according to Equation (9). R_c and T_c can be constructed according to Equation (4).

4.1. Segmental Analysis. The 8th segment (GTS8) in the south section of the target bridge steel pylon was selected to predict its erection posture. As shown in Figure 11, the green part represents the GTS8 segment to be erected, while the blue part refers to the previously erected segments.

Due to the particularity of interface inclination, it is hard to pre-assemble the three segments in the segment prefabrication plant. Therefore, a fitting allowance was reserved for the fabrication of the three segments. In other words, unified processing and adjustment would follow the erection of GTS5 and GTS7 according to the actual interface states, and GTS8 posture prediction results. The deviations in the coordinates of geometric feature points on the upper interfaces of GTS5 and GTS7 segments after welding are shown in Figure 12. The results show that such feature points generally were subject to superelevation and offset in the longitudinal direction (X direction) of bridge. Specifically, the axial center was superelevated by 14 mm, and the offset in the longitudinal direction reached 16 mm.

Initial positioning of GTS8 was performed through the 6D optimal matching between each feature point of GTS8 and the deviation-free erection state. After the objective function was constructed according to Equation (9), the optimal calculation was performed based on the BFGS quasi-Newtonian variable-scale method. The process of improving the objective function value with the iterative calculation is shown in Figure 13. The results show that the initial 83 mm converged to 66 mm after 22 iterative calculations. It is proven that the optimal calculation effectively improved the misalignment between connection interfaces. The deviations between the feature points of lower interfaces of GTS8 and corresponding feature points of erected GTS5 and GTS7 segments, as well as the optimal calculation results are shown in Table 4. The single maximum deviation and mean deviation in the feature points on the connection interfaces of upper and lower segments at the projection plane reached 10 and 5 mm, respectively, indicating the existence of a certain gap. However, the optimal state of misalignment was achieved. The said misalignment is related to many factors such as plate unit manufacturing error, welding shrinkage, and deformation between plate units. In fact, local misalignment and deformation could be adjusted through the thermal rectification process before the formal welding of front and rear segments, to meet the wallboard alignment and welding conditions.

Based on the parameter optimization results, the posture of the segment to be erected in case of optimal misalignment between connection interfaces can be predicted. The calculation result in Figure 14 shows that the maximum axial center deviation of 7 mm in the upper interface of the GTS8 segment is reflected in the central axis direction of bridge (X direction).

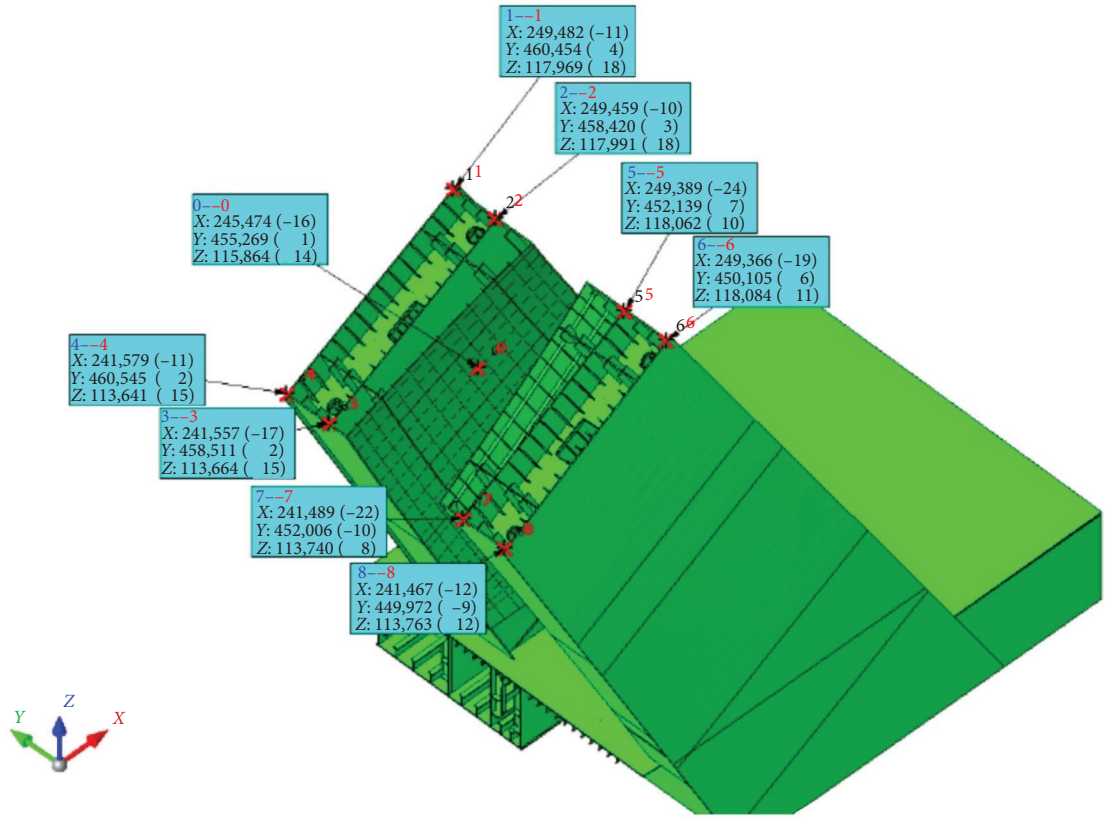

Figure 12: GTS5 and GTS7 coordinate deviation of geometry feature points after erection accomplishment.

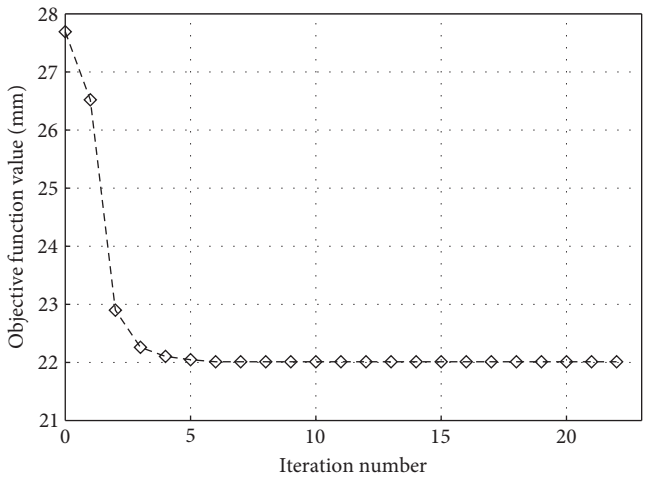

Figure 13: Improvement of objective function values with iterations.

The deviation in the feature points on the upper interface of GTS8 to be erected in case of optimal misalignment between connection interfaces and the feature points with the optimal erection posture, as well as the deviation in the feature points on the lower interface thereof and the feature points of previously erected GTS5 and GTS7 segments. As shown in Table 4, normal overlapping amount reflects the difference between the feature points on the connection interfaces of upper and lower segments in the z direction of the local coordinate system. A negative value indicates the overlapping, that is, the upper and lower segments are too longer than those in the desired state. In contrast, a positive value indicates a gap, that is, the upper and lower segments are too shorter than those in the desired state. In order to ensure that the upper interface of GTS8 can achieve the deviation state indicated, the overlapping area of connection interfaces should be removed. The normal overlapping amount of the corresponding feature points on the connection interface is also the adjustable amount of segment length. Because GTS5 and GTS7 segments had been erected, and GTS8 segment was still in the prefabrication plant, all angular points on the lower interface of GTS8 were cut. The predicted deviation after such cutting is shown in Figure 14, while the actual deviation of the upper interface of GTS8 after processing, adjustment, and erection is shown in Figure 15. The results show that the two deviations are very close, and the maximum deviation in the axial center is only 4 mm. It indicates that the method for segment posture prediction, processing and adjustment is effective to guide the segment erection.

4.2. Pylon Analysis. A rapid positioning of bending–torsion steel pylon of the target bridge by segment was realized based on the said multiple feature points coordinate transfer method that takes into account the deviation in fabrication and erection. Based on the principle of minimizing the

Table 4: Connection interfaces matching state with minimum align deviation value.

Feature point	Erected segment			To be erected segment			Calculated misalignment		Normal superposition
	X	Y	Z	X	Y	Z	X	Y	Z
U1\L1	10,354	2	22	10,350	8	−19	−4	6	−41
U2\L2	8,319	1	21	8,316	11	−8	−2	10	−28
U3\L3	8,368	9,018	21	8,368	9,018	2	0	0	−19
U4\L4	10,403	9,014	18	10,400	9,024	−11	−3	10	−30
U5\L5	2,041	17	21	2,034	8	−7	−7	−9	−28
U6\L6	6	12	19	3	8	0	−2	−4	−19
U7\L7	1,850	9,020	18	1,859	9,011	−3	9	−8	−21
U8\L8	−183	9,008	16	−174	9,011	−8	9	3	−24

Optimization parameters of misalignment: $\Delta X = 3.2$, $\Delta Y = 5.9$, and $\omega_z = -3.93\text{E-}04$.

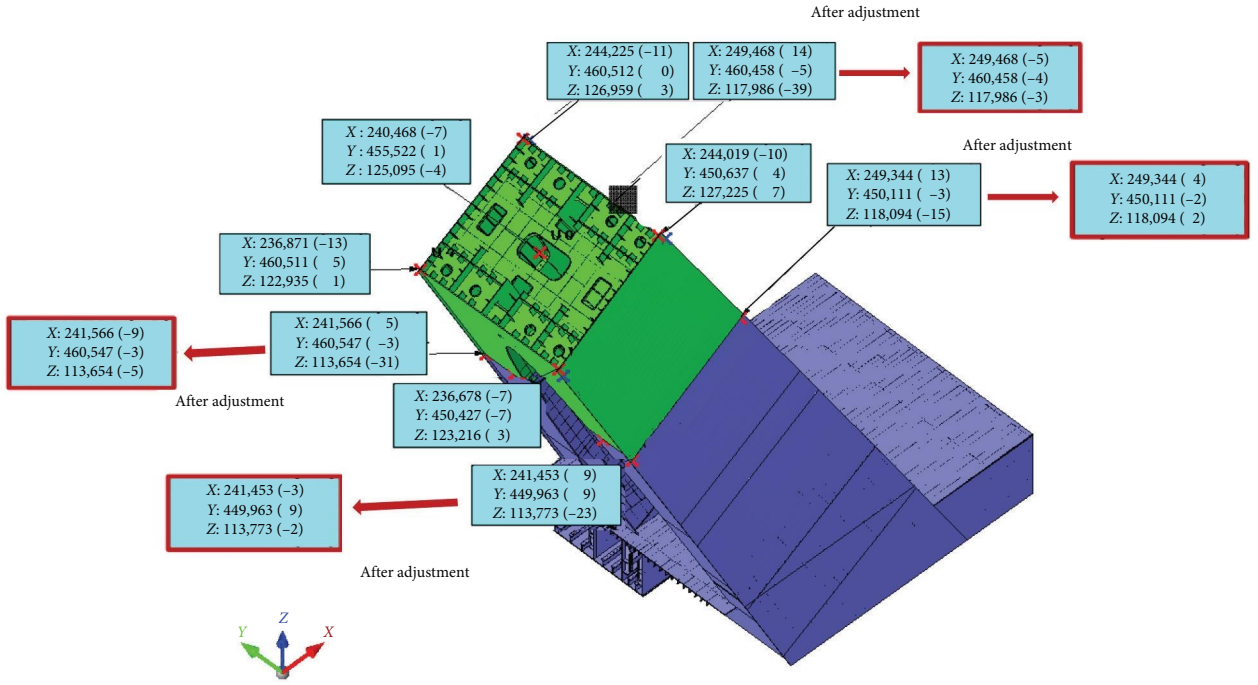

Figure 14: Posture forecast of GTS8 with minimum align deviation value at the lower interface.

planar misalignment between connection interfaces, the posture prediction of the segment to be erected was performed. Results show that this method is effective to guide the segment fabrication, erection, and adjustment. The distribution of the high pylon and the horizontal direction of the bridge is shown in Figure 16; where N refers to the north limb, S refers to the south limb, 0 refers to the unbiased state, U refers to the upper deviation, L refers to the lower deviation, and e refers to the actual deviation. The measured results show that the deviation of the axis of the steel pylon meets the requirement of less than that in the H/4,000.

5. Conclusions

This paper introduced a coordinate transfer method for multiple feature points, aiming to improve the erection precision of arch-shaped, variable-section bending–torsion steel pylons by segment. Through a comprehensive analysis of the measurement error curve and its random distribution, factors influencing the precision of the transfer method were thoroughly assessed to optimize the measurement point layout. Additionally, a predictive method for segment posture was developed, considering fabrication and erection deviations, effectively guiding the construction process. The methods and their application in the construction of high-precision steel towers offer some guidance for the accurate installation and adjustment of complex steel structures. The major conclusions of this study are as follows:

(1) Point layout optimization: The area and angle uniformity of the three-point configuration substantially influence axis coordinate estimation error, with an

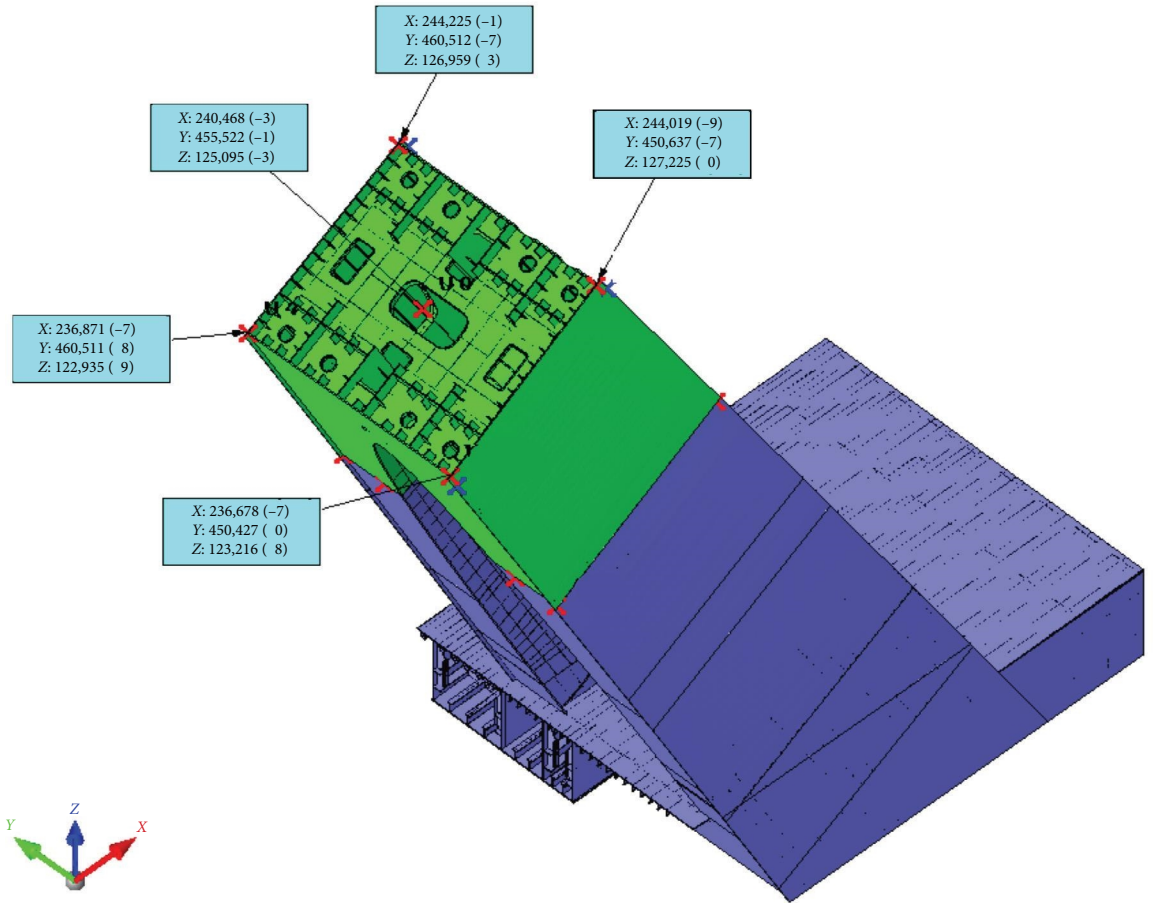

Figure 15: GT8 coordinate deviation of geometry feature points after erection accomplishment.

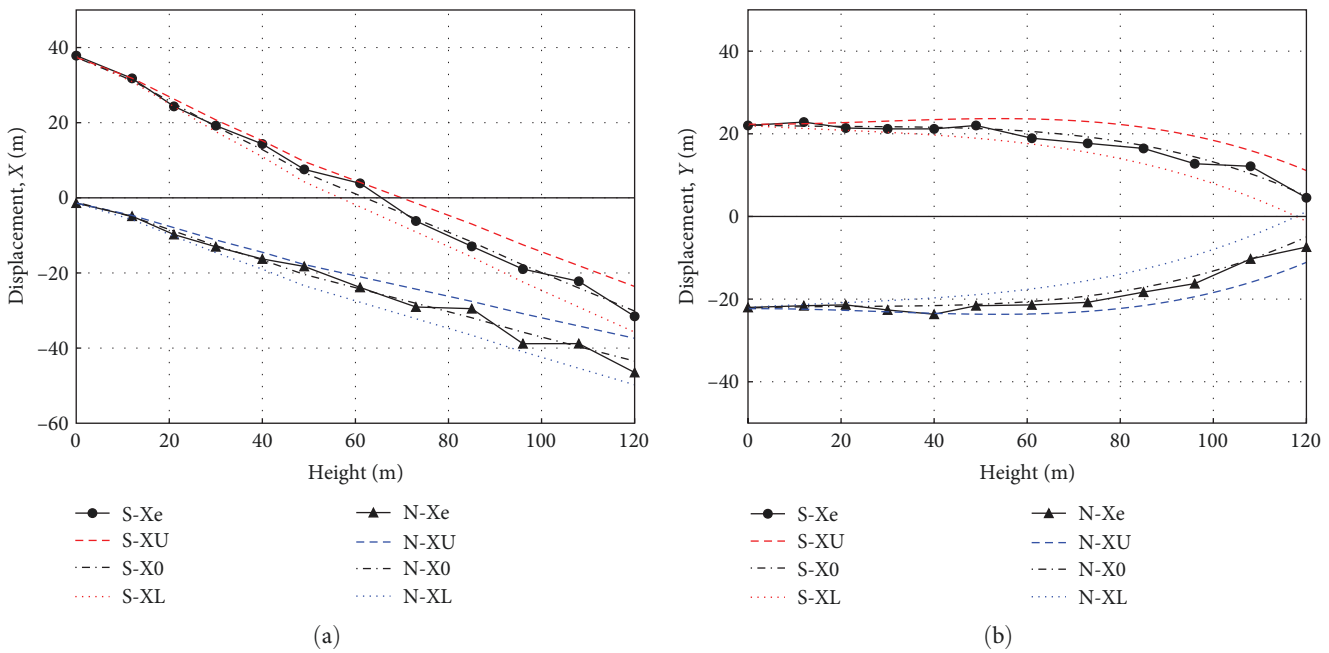

Figure 16: Axis line deviation distribution of high pylon after closure: (a) along the bridge deviation distribution and (b) cross-bridge deviation distribution.

optimized layout achieving a point difference ratio of 1.50 and an absolute deviation of 5.3 mm, meeting high-altitude steel pylon precision requirements.

(2) Posture prediction: Considering both erection and manufacturing deviations, this approach involves plane fitting of connection interface feature points and the establishment of a local coordinate system. The BFGS quasi-Newton optimization algorithm is used to predict and analyze the optimal posture of segments, guiding their processing and adjustment.

(3) Geometry control: Postconstruction, the axis deviation of the background steel pylon conforms to the H/4,000 geometric attitude control standard, underscoring the method's effectiveness.

(4) The coordinate transfer method developed in this study, and its application in the high-precision construction of steel towers, heralds a new wave of innovation in the field of accurate installation and adjustment of the complex structures, especially in large-scale infrastructure and high-rise building construction, bringing about more efficient and cost-effective construction solutions for the industry.

Data Availability

All data, models, or codes that support the findings of this study are available from the corresponding author upon reasonable request.

Conflicts of Interest

The authors declare that there is no conflict of interest regarding the publication of this paper.

Acknowledgments

This research was funded by the Key Research and Development Project of China State Railway Group Company Ltd. (J2023G013) and the Development Project of China Academy of Railway Science Co., Ltd. (2022YJ180).

References

[1] M. S. Mafipour, S. Vilgertshofer, and A. Borrmann, "Automated geometric digital twinning of bridges from segmented point clouds by parametric prototype models," *Automation in Construction*, vol. 156, Article ID 105101, 2023.

[2] W. Du, D. Lei, P. Bai, F. Zhu, and Z. Huang, "Dynamic measurement of stay-cable force using digital image techniques," *Measurement*, vol. 151, Article ID 107211, 2020.

[3] Y. Tian, C. Zhang, S. Jiang, J. Zhang, and W. Duan, "Noncontact cable force estimation with unmanned aerial vehicle and computer vision," *Computer-Aided Civil and Infrastructure Engineering*, vol. 36, no. 1, pp. 73–88, 2021.

[4] Y. Zeng, Y. Zeng, H. Yu, Y. Tan, H. Tan, and H. Zheng, "Dynamic characteristics of a double-pylon cable-stayed bridge with steel truss girder and single-cable plane," *Advances in Civil Engineering*, vol. 2021, Article ID 9565730, 15 pages, 2021.

[5] X. X. Cheng, G. Wu, L. Zhang, and F. B. Ma, "A new damage detection method for special-shaped steel arch bridges based on fractal theory and the model updating technique," *International Journal of Structural Stability and Dynamics*, vol. 21, no. 3, Article ID 2150030, 2021.

[6] E. Watanabe, H. Furuta, T. Yamaguchi, and M. Kano, "On longevity and monitoring technologies of bridges: a survey study by the Japanese Society of Steel Construction," *Structure and Infrastructure Engineering*, vol. 10, no. 4, pp. 471–491, 2014.

[7] C.-S. Huang, Y.-P. Tseng, and C.-J. Lin, "In-plane transient responses of arch with variable curvature using dynamic stiffness method," *Journal of Engineering Mechanics*, vol. 124, no. 8, pp. 826–835, 1998.

[8] R. Cucuzza, C. Costi, M. M. Rosso, M. Domaneschi, G. C. Marano, and D. Masera, "Optimal strengthening by steel truss arches in prestressed girder bridges," in *Proceedings of the Institution of Civil Engineers—Bridge Engineering*, pp. 1–51, ICE Publishing, 2022.

[9] R. Cucuzza, M. M. Rosso, and G. C. Marano, "Optimal preliminary design of variable section beams criterion," *SN Applied Sciences*, vol. 3, no. 8, Article ID 745, 2021.

[10] H. Wang, X. Fang, L. Bai, Z. Zeng, Z. Shang, and Y. Shi, "3D simulation of steel pylon segment preassembly of large scale cable supported bridge," *China Railway Science*, no. 2, pp. 67–71, 2008.

[11] Z. M. Zeidan, A. A. Beshr, and A. G. Shehata, "Study the precision of creating 3D structure modeling form terrestrial laser scanner observations," *Journal of Applied Geodesy*, vol. 12, no. 4, pp. 303–309, 2018.

[12] E. Lambrou, G. Pantazis, and K. Nikolitsas, "Special marking of 3D networks' points for the monitoring of modern constructions," *Journal of Civil Engineering and Architecture*, vol. 5, no. 7, 2011.

[13] Y. Xu, J. M. W. Brownjohn, and F. Huseynov, "Accurate deformation monitoring on bridge structures using a cost-effective sensing system combined with a camera and accelerometers: case study," *Journal of Bridge Engineering*, vol. 24, no. 1, Article ID 05018014, 2019.

[14] H. Tserng, J. Han, C. Lin, M. Skibniewski, and K. Weng, "GPS-based real-time guidance information system for marine pier construction," *Journal of Surveying Engineering*, vol. 139, no. 2, pp. 84–94, 2013.

[15] C. Watson, T. Watson, and R. Coleman, "Structural monitoring of cable-stayed bridge: analysis of GPS versus modeled deflections," *Journal of Surveying Engineering*, vol. 133, no. 1, pp. 23–28, 2007.

[16] C. S. Huang, Y. P. Tseng, A. W. Leissa, and K. Y. Nieh, "An exact solution for in-plane vibrations of an arch having variable curvature and cross section," *International Journal of Mechanical Sciences*, vol. 40, no. 11, pp. 1159–1173, 1998.

[17] E. Tufekci and O. Y. Dogruer, "Exact solution of out-of-plane problems of an arch with varying curvature and cross section," *Journal of Engineering Mechanics*, vol. 132, no. 6, pp. 600–609, 2006.

[18] J. Melchiorre, A. Manuello, F. Marmo, S. Adriaenssens, and G. C. Marano, "Differential formulation and numerical solution for elastic arches with variable curvature and tapered cross-sections," *European Journal of Mechanics—A/Solids*, vol. 97, Article ID 104757, 2023.

[19] T. Huang, G. Li, H. Chen, and M. Jiang, "Precise control survey for erecting the steel pylons of the third Nanjing Yangtze River Bridge, China: case study," *Journal of Surveying Engineering*, vol. 136, no. 1, pp. 29–35, 2010.

[20] W. Dong, "The 3D positioning model and staking-out methods of slope–column in national stadium project," *Bulletin of Surveying and Mapping*, no. 5, pp. 33–37, 2006.
[21] X. Zuo, F. Yang, J. Wu, D. Lou, and J. Jiang, "Several advanced construction techniques for irregular polyhedron steel roof systems," *Journal of Zhejiang University Engineering Science*, vol. 44, no. 1, pp. 145–149, 2010.
[22] S. Wang, Z. Ke, Y. Gao, Y. Li, and B. Yang, "High precision cutting length calculation method and application of special-shaped steel pylon with closure segment," *Journal of Tongji University Natural Science*, vol. 48, no. 3, pp. 358–367, 2020.
[23] S. Wang, Z. Ke, and Y. Gao, "Stiffness parameters identification and erection optimization for temporary fixing system in irregular steel pylon," *Bridge Construction*, vol. 50, no. 1, pp. 55–60, 2020.
[24] Z. Wang, N. Zhang, and S. Wang, "Geometry control of special-shaped arch pylon considering seasonal temperature changes during construction," *Structures*, vol. 36, pp. 416–427, 2022.
[25] Z. Wang, N. Zhang, X. Du, S. Wang, and Q. Sun, "Multiobjective optimization of cable forces and counterweights for universal cable-stayed bridges," *Journal of Advanced Transportation*, vol. 2021, Article ID 6615746, 13 pages, 2021.
[26] The MathWorks, Inc., "Find minimum of constrained nonlinear multivariable function—MATLAB fmincon," https://www.mathworks.com/help/optim/ug/fmincon.html.
[27] L. Zhang, G. Qiu, and Z. Chen, "Structural health monitoring methods of cables in cable-stayed bridge: a review," *Measurement*, vol. 168, Article ID 108343, 2021.
[28] H.-W. Zhao, Y.-L. Ding, A.-Q. Li, B. Chen, and K.-P. Wang, "Digital modeling approach of distributional mapping from structural temperature field to temperature-induced strain field for bridges," *Journal of Civil Structural Health Monitoring*, vol. 13, no. 1, pp. 251–267, 2023.